High Power Laser Science and Engineering, (2022), Vol. 10, e30, 9 pages.
doi:10.1017/hpl.2022.24

HIGH POWER LASER SCIENCE AND ENGINEERING

RESEARCH ARTICLE

A nodule dome removal strategy to improve the laser-induced damage threshold of coatings

Tianbao Liu[1,2], Meiping Zhu[1,2,3,4], Wenyun Du[1,2], Jun Shi[1,2,3], Jian Sun[1,4], Yingjie Chai[5], and Jianda Shao[1,2,3,4]

[1] *Laboratory of Thin Film Optics, Key Laboratory of Materials for High Power Laser, Shanghai Institute of Optics and Fine Mechanics, Chinese Academy of Sciences, Shanghai, China*

[2] *Center of Materials Science and Optoelectronics Engineering, University of Chinese Academy of Sciences, Beijing, China*

[3] *Hangzhou Institute for Advanced Study, University of Chinese Academy of Sciences, Hangzhou, China*

[4] *CAS Center for Excellence in Ultra-intense Laser Science, Shanghai, China*

[5] *CREOL, College of Optics and Photonics, University of Central Florida, Orlando, USA*

(Received 15 August 2022; revised 31 August 2022; accepted 8 September 2022)

Abstract

Various coatings in high-power laser facilities suffer from laser damage due to nodule defects. We propose a nodule dome removal (NDR) strategy to eliminate unwanted localized electric-field (E-field) enhancement caused by nodule defects, thereby improving the laser-induced damage threshold (LIDT) of laser coatings. It is theoretically demonstrated that the proposed NDR strategy can reduce the localized E-field enhancement of nodules in mirror coatings, polarizer coatings and beam splitter coatings. An ultraviolet (UV) mirror coating is experimentally demonstrated using the NDR strategy. The LIDT is improved to about 1.9 and 2.2 times for the UV mirror coating without artificial nodules and the UV mirror coating with artificial nodule seeds with a diameter of 1000 nm, respectively. The NDR strategy, applicable to coatings prepared by different deposition methods, improves the LIDT of laser coating without affecting other properties, such as the spectrum, stress and surface roughness, indicating its broad applicability in high-LIDT laser coatings.

Keywords: coating; electric-field enhancement; laser-induced damage threshold; nodule defect; nodule dome removal

1. Introduction

Laser coatings are one of the key components in laser systems, such as inertial confinement fusion lasers, ultra-intense and ultra-short lasers and high-energy lasers[1–4]. Many coatings used in ultraviolet (UV) to near-infrared (NIR) lasers, including mirror coatings[5–7], polarizer coatings[8,9] and beam-splitting coatings[10,11], suffer from laser damage due to nodule defects. Nodule defects grow from particles on the substrate surface and/or particles generated during the coating deposition process into inverted cones with domed tops[12–14], resulting in unwanted localized electric-field (E-field) enhancement and coating layer discontinuities[6,15,16]. The reported micro-lens model and angular-dependent transmission model suggest that localized E-field enhancement can lead to nodule ejection under laser irradiation[17,18]. Although several works have been devoted to eliminating nodules[19–21], nodules are unavoidable in laser coatings. Traditionally, laser conditioning[22,23] and nodule planarization[24] methods are used to reduce the adverse effects of nodule defects. However, laser conditioning produces plasma scalds and nodule-ejected pits[25], requiring a trade-off between the laser-induced damage threshold (LIDT) and the surface quality of the coating; nodule planarization is limited to ion-beam sputtering deposition, not e-beam evaporation – a technique especially suitable for large, high-power laser optics.

Here, we propose a nodule dome removal (NDR) strategy to eliminate the unwanted localized E-field enhancement caused by nodule defects, thereby improving the LIDT of laser coatings. First, the reduction of localized E-field enhancement in mirror coatings, polarizer coatings and beam-splitter coatings by removing nodule domes is theoretically investigated using the finite-element method (FEM)[7]. Then, a UV laser mirror coating with artificial nodule seeds is prepared, and nodule domes are experimentally removed

Correspondence to: M. Zhu, Shanghai Institute of Optics and Fine Mechanics, Chinese Academy of Sciences, Shanghai 201800, China. Email: bree@siom.ac.cn

by the NDR process. As we will show, this NDR strategy can reduce the localized E-field enhancement and improve the LIDT of laser coatings without degrading other properties of the coating, such as the spectrum, stress and surface roughness. We believe that our NDR strategy can benefit various laser coatings prepared by different deposition techniques.

2. Simulation

The E-field distributions of nodules without domes in a mirror coating (HR), a polarizer coating (POL) and a plate laser beam splitter coating (PLBS) are investigated by FEM simulation. For comparison, the E-field distribution of nodules with domes in the corresponding coatings is calculated. The design structures and theoretical reflectance spectra of the coatings are shown in Table 1 and Figure 1(a), respectively. The geometry of the nodule used for FEM simulation is described by $D = \mathrm{sqrt}(4dt)$[26], where D is the diameter of the nodule dome, d is the diameter of the spherical seed and t is the depth of the seed, as shown in Figure 1(b). Here, d is set to 550 nm in all coatings, and t and D are calculated and listed in Table 1.

The E-field distributions of nodules with and without domes in HR, POL and PLBS coatings are compared in Figure 1(c). For all coatings, the localized E-field enhancement is significantly reduced in nodules without domes compared to nodules with domes, especially in the high refractive index (n) layer, which is more prone to damage under laser irradiation due to its relatively smaller band

Table 1. Design structures of the coatings.

Sample	Design structure	Reference wavelength (nm)	Refractive index (n)		t (nm)	D (nm)
			n_H	n_L		
HR	Substrate $\|2L_1(H_1L_1)^{18}H_1 8.15L_1\|$Air	1187	1.653	1.437	9224	4505
POL	Substrate $\|2L_2(H_2L_2)^7 0.5H_2L_2 0.5H_2L_2\ (H_2L_2)^7$ $0.45H_2 3.5L_2\|$Air	1064	2.030	1.438	6002	3634
PLBS	Substrate $\|2L_3H_3L_3H_3 2L_3\|$Air	1187	1.834	1.437	1356	1727

Note: H_i and L_i represent the high-n layer and low-n layer with a quarter-wavelength optical thickness (QWOT) at the reference wavelength, respectively.

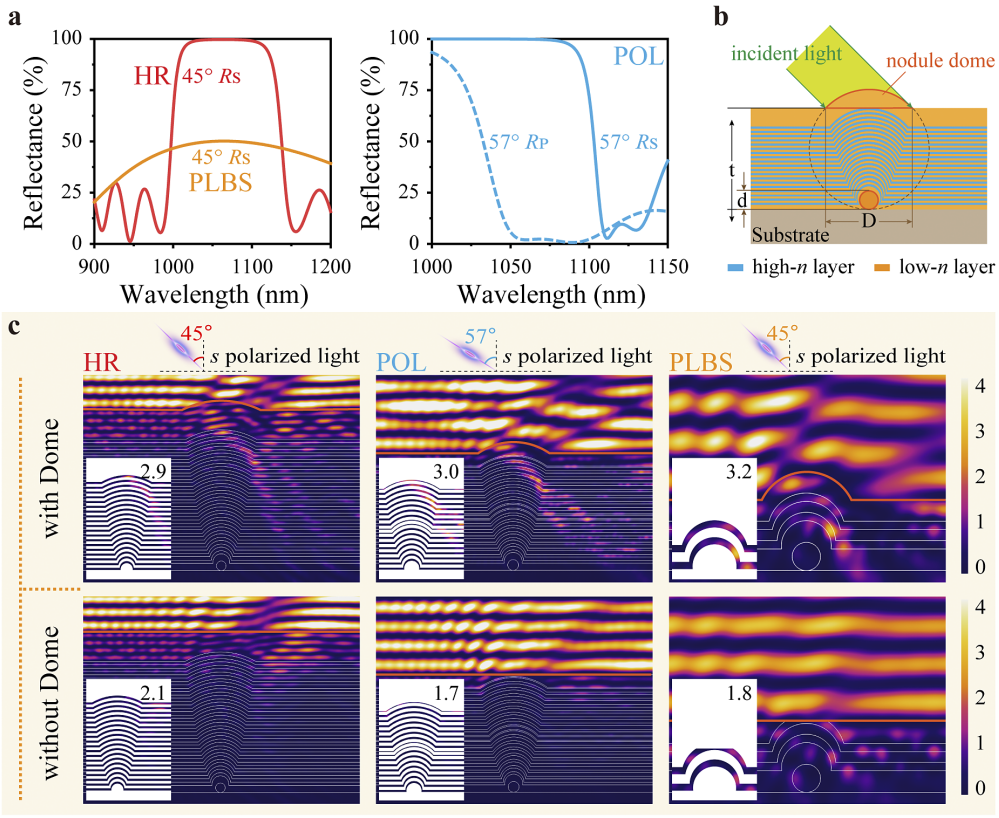

Figure 1. (a) Theoretical reflectance spectra of a mirror coating (with an incident angle of 45°), a plate laser beam splitter coating (with an incident angle of 45°) and a polarizer coating (with an incident angle of 57°). (b) Geometry of the $D = \mathrm{sqrt}(4dt)$ nodule. (c) Simulated E-field distributions for the nodules with and without domes (with an incident light with a wavelength of 1064 nm). The inset shows the E-field distribution in high-n layers, and the peak E-field intensity values are given.

https://doi.org/10.1017/hpl.2022.24 Published online by Cambridge University Press

gap[27]. The maximum E-field intensity in the high-n layer is shown in the inset of Figure 1(c). Simulation results show that the proposed NDR strategy can reduce the localized E-field enhancement of nodules in various coatings. The NDR strategy may be a good solution to improve the LIDT of coatings with initial damage closely related to nodule-induced E-field enhancement.

3. Experimental details

3.1. Preparation of artificial nodules

Spherical nodule seeds with diameters of 200, 550, 750 and 1000 nm are pre-planted on the surface of BK7 substrates using the following steps. First, the seeds are dispersed in anhydrous ethanol for 15 minutes by ultrasonic treatment. Next, the ethanol suspension is heated to 60°C and left to stand for 10 minutes. Then, the substrate is immersed vertically in the ethanol suspension for 1 minute. Finally, the substrate is removed from the ethanol suspension and the liquid is quickly blotted from the edge of the substrate with a cleanroom wiper. Here, the nodule seeds with a diameter of 200 nm are gold particles, while the nodule seeds with other diameters are monodisperse silica. For the mirror coating used at an angle of incidence of 45° in this work, no matter whether the seeds are gold particles or silica spheres, the E-field distribution at the nodule defects shows little difference. A nodule areal density of 30–50 mm^{-2} is achieved by adjusting the concentration of the ethanol suspension containing silica or gold microspheres, resulting in nodules under each laser shot when performing LIDT measurement.

3.2. Preparation of mirror coatings

A UV mirror coating consisting of alternating Al_2O_3–HfO_2 mixture layers and SiO_2 layers is deposited by electron-beam (e-beam) evaporation. The Al_2O_3–HfO_2 mixture layer is deposited by dual-source e-beam co-evaporation of Al_2O_3 and metal Hf. All coating interfaces are co-evaporated interfaces described elsewhere[5]. Prior to deposition, the coating chamber is heated to 200°C and evacuated to a base pressure lower than 5×10^{-4} Pa. The deposition rates of Al_2O_3 and HfO_2 in the mixture layer are 0.07 and 0.03 nm/s, respectively. The SiO_2 layer is evaporated from SiO_2 at a deposition rate of 0.20 nm/s. The oxygen pressures for the deposition of Al_2O_3–HfO_2 mixture and SiO_2 layers are 1.8×10^{-2} and 5×10^{-3} Pa, respectively.

3.3. Nodule dome removal process

The NDR process consists of six steps, as shown in Figure 2. Step 1 is cleaning. The polishing pad – a single-side polished silicon wafer with a root-mean-square (RMS) surface roughness less than 0.5 nm – is ultrasonically cleaned with deionized water for 5 minutes to obtain a clean polishing surface. Step 2 is wetting. Anhydrous ethanol is added to the polishing pad, and the ethanol diffuses rapidly due to its excellent wettability with the silicon wafer. Step 3 is main polishing. The coating is placed on the polishing pad to form a uniform ethanol liquid film between the pad surface and the coating surface. The coating is pushed to rotate at a constant speed on the surface of the polishing pad. During the rotation process, the liquid film is gradually thinned, the gradually increasing capillary force[28] between the coating and the polishing pad acts as a normal load and the nodule dome is gradually polished by friction[29]. Step 4 is cleaning. The polishing pad is ultrasonically cleaned while rinsing the coating surface with deionized water for 5 minutes to partially remove the debris generated in step 3. Step 5 is fine polishing. The coating is placed on the polishing pad and pushed to rotate in a flowing deionized water environment for 5 minutes to remove residual debris. Step 6 is drying.

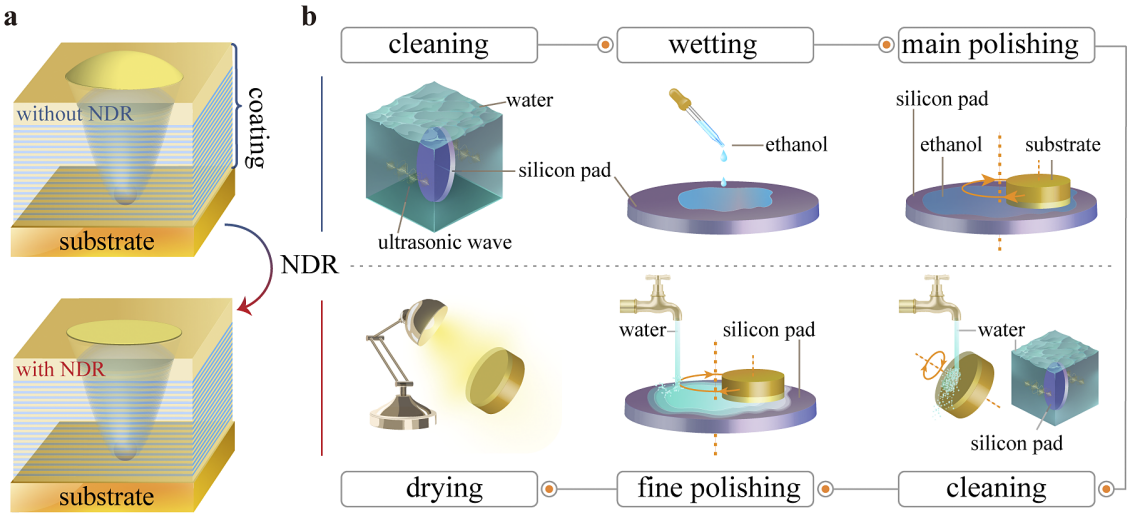

Figure 2. Schematic illustration of the proposed NDR process. (a) A nodule defect without and with the NDR process. (b) The six steps of the NDR process.

https://doi.org/10.1017/hpl.2022.24 Published online by Cambridge University Press

The coating is dried with a lamp. In the proposed NDR process, anhydrous ethanol is used instead of the polishing powder used in traditional polishing methods[30,31], thus avoiding possible surface scratches to the coating.

3.4. Characterization of mirror coatings

The transmittance spectrum of the coating is measured by a spectrometer (Lambda 1050 UV/VIS/NIR, Perkin-Elmer), and the reflectance spectrum is calculated from the transmittance data, neglecting absorption. The RMS roughness is characterized by an atomic force microscope (AFM, Veeco Dimension-3100) in tapping mode with a scan area of 5 μm × 5 μm. The sample surface profile of the coating is characterized by an optical interferometer (ZYGO Mark III-GPI) in a controlled environment with a temperature of 23°C ± 1.5°C and relative humidity of 45% ± 5%. The surface and cross-section morphologies of the coating at the nodules are obtained by a focused ion-beam scanning electron microscope (FIB-SEM, Carl Zeiss AURIGA CrossBeam). The one-on-one LIDT measurement is performed by the method described in the ISO 21254 standard, using an s-polarized 3ω Nd:YAG laser with a pulse width of 8 ns and an angle of incidence of 45°. The effective beam size on the sample surface is about 0.30 mm^2, and 15 sites are tested for each laser fluence.

4. Results and discussion

4.1. Properties of UV mirror coatings without and with the NDR process

A UV mirror coating with a layered structure of substrate/2L(ML)^{18}M8.15L/air is designed to achieve an s-polarized reflectance higher than 99.5% at 355 nm at an angle of incidence of 45°. M and L represent Al_2O_3–HfO_2 mixture and SiO_2 layers with a quarter-wavelength optical thickness (QWOT) at 395 nm, respectively. The atomic

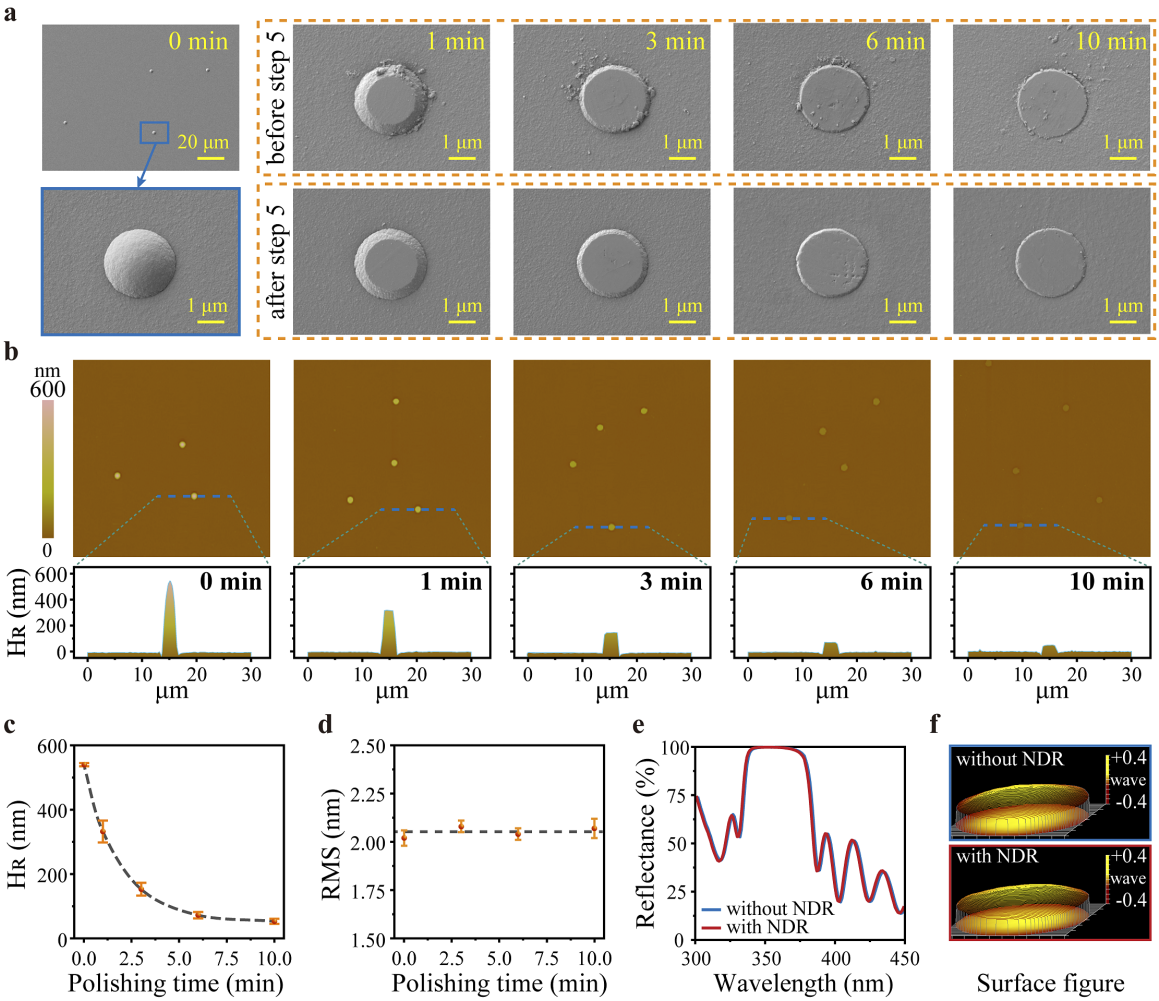

Figure 3. Morphologies and optical properties of mirror coatings without and with the NDR process. (a) SEM characterized morphologies of the nodule domes with different polishing times. (b) AFM characterized morphologies of the mirror coating with different polishing times. (c) Residual height of the nodule dome versus polishing time. (d) RMS roughness, (e) reflectance spectra (measured at an incident angle of 45°, s-polarized light) and (f) surface figure of the mirror coating without and with the NDR process. Error bars in (c) and (d) describe the values measured at different areas of the coating.

https://doi.org/10.1017/hpl.2022.24 Published online by Cambridge University Press

content ratio of Al and Hf in the Al_2O_3–HfO_2 mixture layer is about 2.28:1. The n values of M and L at 395 nm are 1.709 and 1.459, respectively.

The surface morphologies of the nodules (seed diameter: 550 nm) after different polishing times are shown in Figures 3(a) and 3(b). The polishing time here and later refers to the main polishing time of step 3 in the NDR process. For nodules before the fine polishing step (step 5), debris of the nodule dome is observed near the nodule, and most of the debris can be removed by step 5 (Figure 3(a)). The height of the nodule dome is reduced from approximately 540 nm to 53 ± 8 nm after a polishing time of 10 minutes. Figure 3(c) shows the residual height of the nodule dome as a function of polishing time. The effect of the NDR process on the surface roughness, spectrum and surface figure of the mirror coating is studied by using a mirror coating without artificial nodule defects. RMS roughness (Figure 3(d)) of the mirror coating does not show a significant change within the polishing time we investigated. After polishing for 10 minutes, no obvious changes are observed in the reflectance spectrum (Figure 3(e)) or surface figure (Figure 3(f)) of the mirror coating.

4.2. Laser-induced damage threshold of mirror coatings

The laser damage probabilities of the mirror coatings without the NDR process as a function of input laser fluence are compared in Figure 4(a). For the mirror coating with artificial nodule seeds with a diameter of 200 nm, the damage probability is close to that of the mirror coating without artificial nodules. As the nodule seed diameter increases, the LIDTs of the mirror coating decrease. The laser damage probability curves of the mirror coatings without and with the NDR process are compared in Figures 4(b)–4(f). Mirror coatings with an artificial nodule seed diameter more than or equal to 550 nm and without the NDR process show a damage probability curve that can be explained by the presence of one type of defect. Other mirror coatings show a damage probability curve that can be explained by the presence of two types of defects with different LIDTs. The model developed by Krol *et al.*[32] is used to extract the defect parameters. If we assume the existence of one class of defects in mirror coatings with artificial nodule seed diameters more than or equal to 550 nm and without the NDR process, and assume the existence of two classes of defects in other mirror coatings, we obtain the results shown in Table 2. Here, D_i, T_i and ΔT_i represent the area defect density (integrated over the thickness), LIDT and the standard deviation of the LIDT, respectively. Overall, the LIDT of the mirror coatings is improved by about 1.6–2.2 times after adopting the NDR process. Among them, the LIDTs of the mirror coating without artificial nodules and the mirror coating with artificial nodule seeds with a diameter of 1000 nm are improved by about 1.9 and 2.2 times, respectively.

4.3. E-field intensity distributions and laser-induced damage morphologies

For coatings with artificial nodule seed diameters more than or equal to 550 nm and no NDR process, only nodule-related

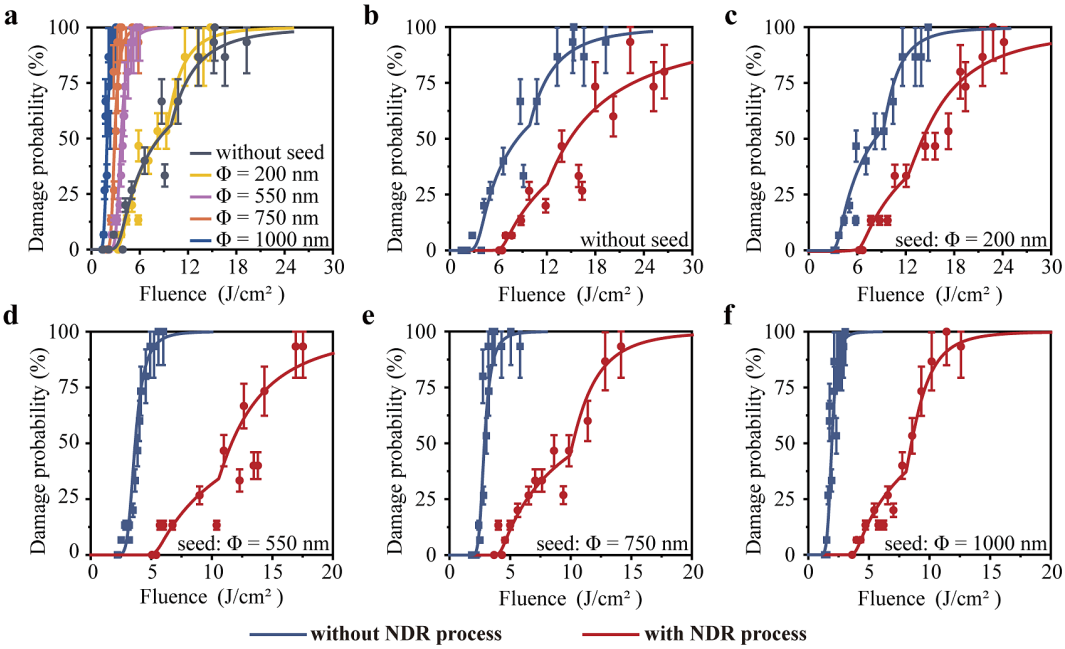

Figure 4. Laser-induced damage probability. Single-pulse damage probability as a function of the input fluence for (a) all mirror coatings without the NDR process, mirror coatings deposited on substrates with (b) no artificial nodule defects and artificial nodule defects with seed diameters of (c) 200 nm, (d) 550 nm, (e) 750 nm and (f) 1000 nm. Error bars describe the relative error of damage probability, including sample-to-sample uncertainty, measurement error of the laser spot area and fluctuations in laser energy[33].

https://doi.org/10.1017/hpl.2022.24 Published online by Cambridge University Press

Table 2. Extracted defect parameters of mirror coatings without and with the NDR process.

Seed diameter (nm)	d_1 (mm^{-2})		T_1 (J/cm^2)		ΔT_1 (J/cm^2)		d_2 (mm^{-2})		T_2 (J/cm^2)		ΔT_2 (J/cm^2)	
	A	B	A	B	A	B	A	B	A	B	A	B
0	5.4	3.8	3.5	6.5	1.0	1.0	23.0	11.0	7.8	9.8	2.0	2.0
200	6.0	4.2	3.6	6.4	0.8	0.8	33.0	14.0	8.1	9.5	2.0	2.0
550	38.0	4.1	3.3	5.4	0.7	0.7		22.0		9.3		2.0
750	41.0	4.6	2.6	4.2	0.5	0.5		35.0		9.0		2.0
1000	43.0	4.3	1.8	3.9	0.5	0.5		42.0		7.8		2.0

Note: A and B represent mirror coatings without the NDR process and mirror coatings with the NDR process, respectively.

damage morphology is observed, which is consistent with the defect parameters extracted in Table 2. For coatings with an artificial nodule seed diameter of 550 nm and no NDR process, typical damage morphologies under different input laser fluences are shown in Figure 5. The E-field distribution at the nodule is investigated by FEM simulation to study the laser-induced damage mechanism. An FIB-characterized cross-sectional image of the nodule in the mirror coating is used as input for simulation. The boundary between the nodule and the surrounding coating is often discontinuous due to self-shadowing effects, and the discontinuity increases with increasing seed diameter. The boundary discontinuity is ignored when we extract the nodule geometry from the measured cross-sectional images. The residual height of the nodule dome in the simulation is 50 nm, which is close to the residual height of the nodule dome in the experimental samples. An s-polarized light with a wavelength of 355 nm illuminates the mirror coating at an angle of incidence of 45°, and the direction of incident light is illustrated in Figure 5. For an illumination fluence near the LIDT, damage occurs in the top-right of the nodule (Figure 5(f)), on the side opposite to the direction of the incident light. The FEM simulation shows that in the top region of the nodule, there is an E-field enhancement in the left-hand side of the outermost low-n layer and in the right-hand side of the neighbouring high-n layer. Although the E-field enhancement of the low-n layer is higher, the high-n layer with enhanced E-field is more prone to damage under laser irradiation due to the smaller band gap of the high-n material. Two localized peak E-field intensity values in high-n layers are given in Figure 5(e). The damage morphology shows traces of material melting, indicating that considerably high temperatures are generated during the laser-induced damage process, and the resulting high tensile stress leads to micro-cracks. At higher input laser fluence, the top few layers of the nodule are lifted (Figure 5(g)). With a further increase in laser fluence, the

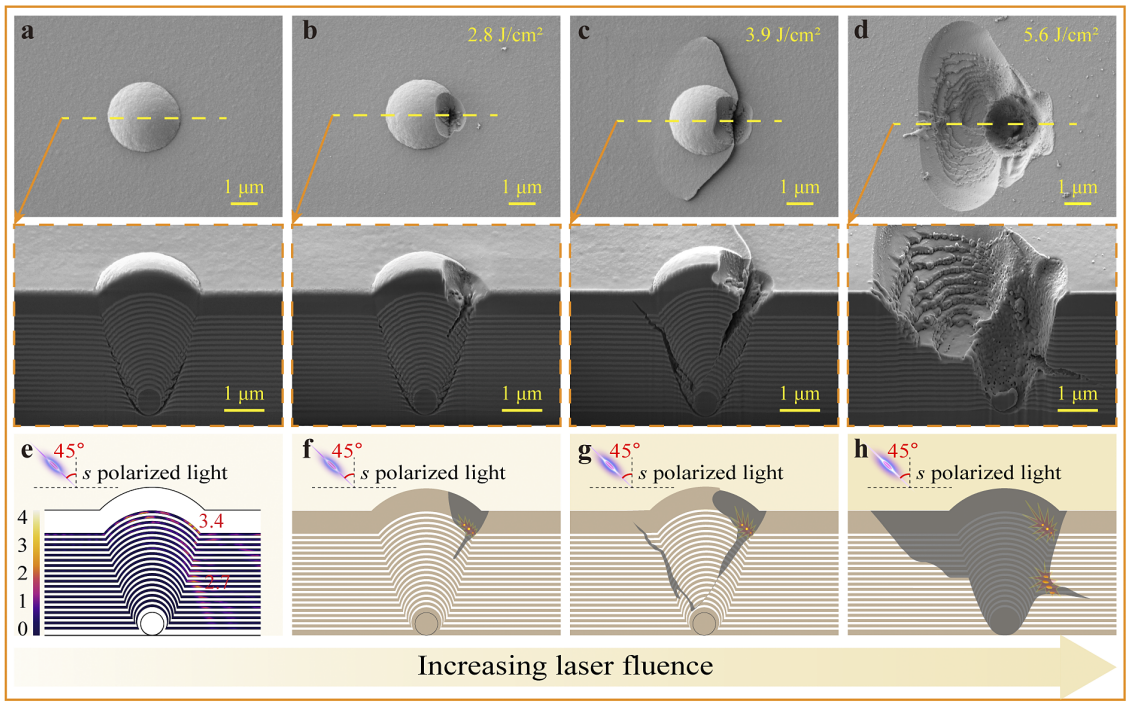

Figure 5. Morphologies of nodules (seed diameter: 550 nm) in the coating without the NDR process. (a) Surface and cross-sectional morphologies of a nodule. Surface and cross-sectional morphologies at the nodules after laser irradiation with fluences of (b) 2.8 J/cm^2, (c) 3.9 J/cm^2 and (d) 5.6 J/cm^2. (e) The E-field intensity distribution in high-n layers. (f)–(h) Schematic diagram of the simulated damage morphologies for increasing laser fluence.

https://doi.org/10.1017/hpl.2022.24 Published online by Cambridge University Press

entire nodule is ejected. Micro-cracks are also observed in the middle of the right-hand boundary of the nodule (Figure 5(h)).

For coatings with the NDR process, two morphological features are observed. One morphological feature is related to nodules observed at fluence slightly higher than the LIDT. The second morphological feature, a flat-bottom pit unrelated to the nodule, is observed as input laser fluence increases. Figure 6 shows typical damage morphologies of nodules (seed diameter: 550 nm) in coatings with the NDR process. The E-field distribution and the peak value in high-*n* layers are given in Figure 6(e). The peak value in high-*n* layers of the nodule with the NDR process is smaller than that of the nodule without the NDR process, and the E-field enhancement area within the nodule with the NDR process is smaller. Consequently, the coating with the NDR process shows improved damage resistance compared with the coating without the NDR process. The initial damage starts from the top-left of the nodule, and the damaged area and depth increase with the laser fluence (Figures 6(f)–6(h)).

The E-field distribution and damage morphology of nodules (with different seed diameters) in coatings without and with the NDR process are compared in Figure 7. Overall, for coatings without the NDR process, the localized E-field enhancement is mainly concentrated in the top region of the nodule and the middle region of the right-hand boundary of the nodule (as highlighted in Figure 7(a)), and the peak E-field intensity value at the nodule increases with increasing seed diameter. For the coating with the NDR process, the localized E-field enhancement at the nodule is obviously reduced (Figure 7(c)), especially in high-*n* layers of the nodule (both the peak value and the E-field enhancement area within the nodule are smaller). The peak E-field intensities of nodules in coatings without and with the NDR process are compared in Table 3.

Typical damage morphology of nodules in coatings without the NDR process shows that most of the layers in the nodule area are ejected along the nodule boundary under laser irradiation. Micro-cracks are observed in the middle region of the right-hand boundary of the nodule (as highlighted in Figure 7(b)), corresponding to the E-field enhancement region in the FEM simulation. Nodules with a seed diameter of 200 nm present unique differences in damage morphology, with several layers damaged in the top-right region of the nodule, which is consistent with the E-field enhancement region. Typical damage morphology of nodules in coatings with the NDR process is shown in Figure 7(d). For nodules with a seed diameter of 200 nm, the damage morphology is similar to that in coatings without the NDR process, except that most of the layers in the nodule area are not ejected. For nodules with seed diameters larger than 200 nm, the damage starts at the top-left region of the nodule, corresponding to the localized E-field enhancement in the high-*n* layers. The insets of Figures 7(b) and 7(d) show the E-field distribution in the high-*n* layers around the micro-crack and the damage area, respectively.

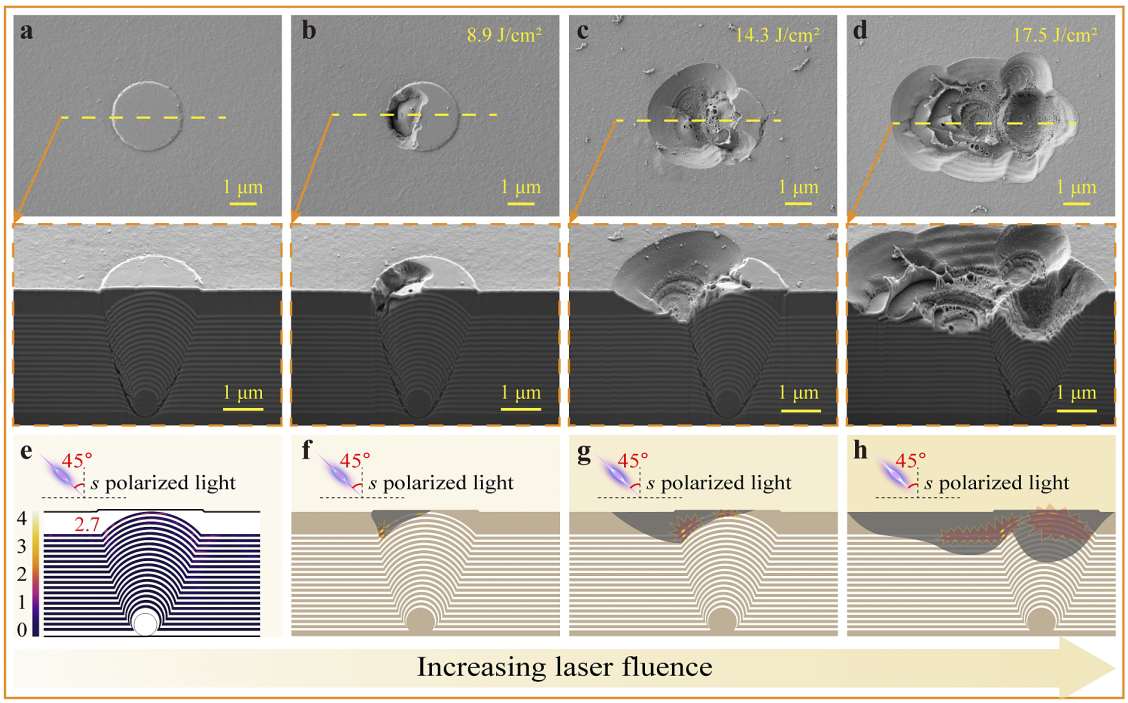

Figure 6. Morphologies of nodules (seed diameter: 550 nm) in the coating with the NDR process. (a) Surface and cross-sectional morphologies of a nodule. Surface and cross-sectional morphologies at the nodules after laser irradiation with fluences of (b) 8.9 J/cm^2, (c) 14.3 J/cm^2 and (d) 17.5 J/cm^2. (e) The E-field intensity distribution in high-*n* layers. (f)–(h) Schematic diagram of the simulated damage morphologies for increasing laser fluence.

https://doi.org/10.1017/hpl.2022.24 Published online by Cambridge University Press

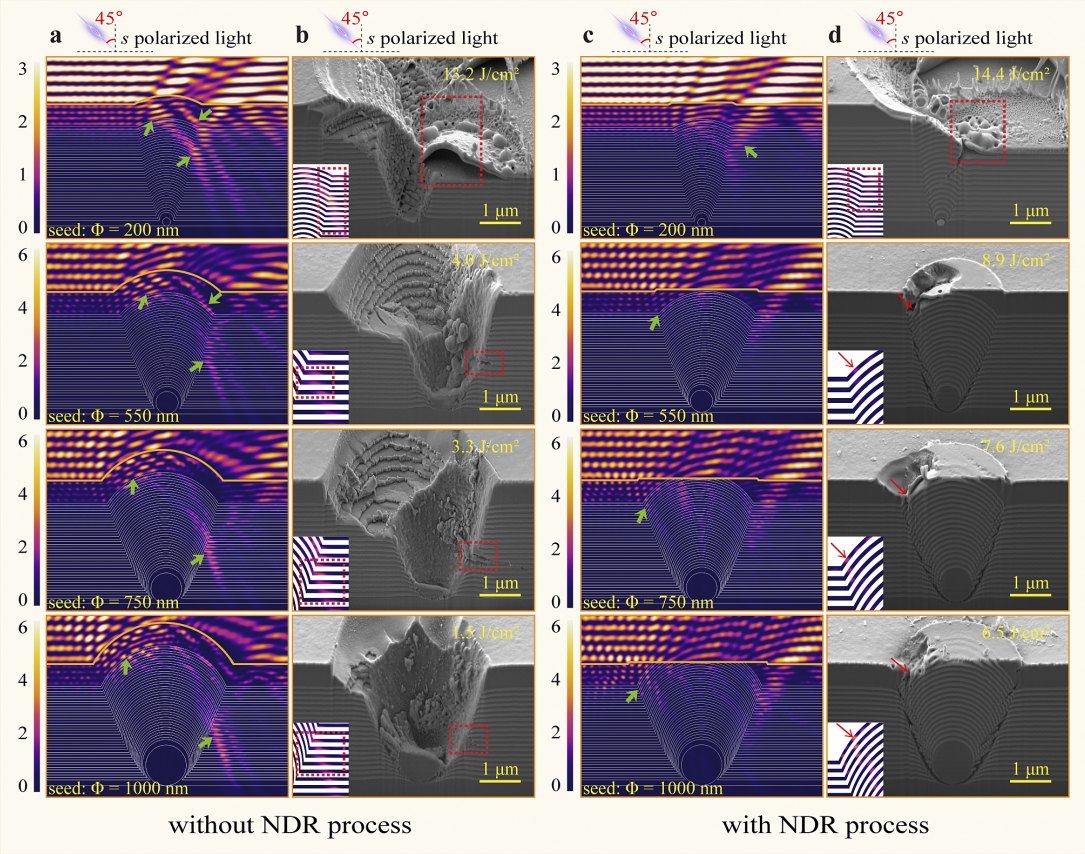

Figure 7. Simulated E-field distributions and damage morphologies of nodules in coatings without and with the NDR process. (a) Simulated E-field distributions and (b) typical damage morphologies of nodules in coatings without the NDR process. (c) Simulated E-field distributions and (d) typical damage morphologies of nodules in coatings with the NDR process. Insets show the E-field distribution in high-*n* layers around the micro-crack and the damage area.

Table 3. Maximum E-field intensity values for nodules with different seed diameters.

Seed diameter	200 nm		550 nm		750 nm		1000 nm	
	L	M	L	M	L	M	L	M
Without NDR	3.9	2.4	6.3	3.4	6.4	3.5	6.9	5.3
With NDR	3.0	1.9	4.1	2.7	4.1	2.8	4.5	4.1

5. Conclusion

In conclusion, we propose an NDR strategy to reduce the localized E-field enhancement of nodule defects, thereby improving the LIDT of laser coatings. It is theoretically demonstrated that the proposed NDR strategy can reduce the localized E-field enhancement of nodules in mirror coatings, polarizer coatings and beam splitter coatings. A UV mirror coating is then experimentally demonstrated using the NDR strategy. The LIDT is improved by about 1.9 and 2.2 times for the UV mirror coating without artificial nodules and the UV mirror coating with artificial nodule seeds with a diameter of 1000 nm, respectively. Typical damage morphologies of mirror coatings suggest that the improvement in the LIDT is largely due to the NDR strategy reducing the local E-field enhancement caused by nodule defects. Our proposed strategy involves only a simple polishing process, and is applicable to coatings prepared by different deposition methods. It can improve the LIDT of laser coating without affecting the other properties, such as the spectrum, stress and surface roughness. We believe that the proposed method can benefit many areas of laser technology where high-LIDT laser coatings play a key role.

Acknowledgements

The authors express their appreciation to Mr Longsheng Wang, Prof. Yuanan Zhao and Mrs Ziyuan Xu for their assistance in sample preparation and LIDT measurement, respectively. This work was supported by the National Natural Science Foundation of China (61975215), the Youth Innovation Promotion Association of the Chinese Academy of Sciences, Strategic Priority Research Program of the Chinese Academy of Sciences (XDA25020206) and the Science

https://doi.org/10.1017/hpl.2022.24 Published online by Cambridge University Press

and Technology Planning Project of Shanghai Municipal Science & Technology Commission (21DZ1100400).

References

1. P. Norvig, D. A. Relman, D. B. Goldstein, D. M. Kammen, D. R. Weinberger, L. C. Aiello, G. Church, J. L. Hennessy, J. Sachs, A. Burrows, G. P. Pisano, J. R. Goldstein, P. Anastas, R. Klausner, D. Baltimore, D. R. Montgomery, T. M. Baer, N. P. Bigelow, R. D. Holt, and J. K. Nicholson, Nature **463**, 26 (2010).
2. R. Betti and O. A. Hurricane, Nat. Phys. **12**, 435 (2016).
3. J. Q. Zhu, J. Zhu, X. C. Li, B. Q. Zhu, W. X. Ma, X. Q. Lu, W. Fan, Z. G. Liu, S. L. Zhou, G. Xu, G. W. Zhang, X. L. Xie, L. Yang, J. F. Wang, X. P. Ouyang, L. Wang, D. W. Li, P. Q. Yang, Q. T. Fan, M. Y. Sun, C. Liu, D. A. Liu, Y. L. Zhang, H. Tao, M. Z. Sun, P. Zhu, B. Y. Wang, Z. Y. Jiao, L. Ren, D. Z. Liu, X. Jiao, H. B. Huang, and Z. Q. Lin, High Power Laser Sci. Eng. **6**, e55 (2018).
4. R. F. Service, Science **301**, 154 (2003).
5. T. T. Zeng, M. P. Zhu, Y. J. Chai, J. P. Li, and J. D. Shao, Photonics Res. **9**, 229 (2021).
6. X. B. Cheng, J. L. Zhang, T. Ding, Z. Y. Wei, H. Q. Li, and Z. S. Wang, Light Sci. Appl. **2**, e80 (2013).
7. M. P. Zhu, N. Xu, B. Roshanzadeh, S. T. P. Boyd, W. Rudolph, Y. J. Chai, and J. D. Shao, Light Sci. Appl. **9**, 20 (2020).
8. M. P. Zhu, K. Yi, Z. X. Fan, and J. D. Shao, Appl. Surf. Sci. **257**, 6884 (2011).
9. J. L. Zhang, Y. J. Xie, X. B. Cheng, T. Ding, and Z. S. Wang, Appl. Opt. **52**, 1512 (2013).
10. W. Y. Du, M. P. Zhu, J. Shi, T. B. Liu, T. T. Zeng, J. Sun, K. Yi, and J. D. Shao, Opt. Laser Technol. **155**, 108399 (2022).
11. Q. Zhou, P. Ma, F. M. Qiu, Y. T. Pu, Z. Qiao, L. Lv, M. X. Zhang, and J. H. Die, Opt. Mater. **125**, 111894 (2022).
12. M. J. Brett, R. N. Tait, S. K. Dew, S. Kamasz, A. H. Labun, and T. Smy, J. Mater. Sci.-Mater. Electron. **3**, 64 (1992).
13. H. J. Qi, M. P. Zhu, M. Fang, S. Y. Shao, C. Y. Wei, K. Yi, and J. D. Shao, High Power Laser Sci. Eng. **1**, 36 (2013).
14. X. F. Liu, D. W. Li, Y. A. Zhao, X. Li, and J. D. Shao, Appl. Surf. Sci. **256**, 3783 (2010).
15. H. P. Ma, X. B. Cheng, J. L. Zhang, H. F. Jiao, B. Ma, Y. J. Tang, Z. L. Wu, and Z. S. Wang, Opt. Lett. **42**, 478 (2017).
16. Y. T. Pu, P. Ma, L. Lv, M. X. Zhang, Z. W. Lu, Z. Qiao, and F. M. Qiu, Appl. Surf. Sci. **440**, 288 (2018).
17. X. B. Cheng, A. Tuniyazi, Z. Y. Wei, J. L. Zhang, T. Ding, H. F. Jiao, B. Ma, H. Q. Li, T. B. Li, and Z. S. Wang, Opt. Express **23**, 8609 (2015).
18. X. B. Cheng, T. He, J. L. Zhang, H. F. Jiao, B. Ma, and Z. S. Wang, Opt. Lett. **42**, 2086 (2017).
19. R. Chow, S. Falabella, G. E. Loomis, F. Rainer, C. J. Stolz, and M. R. Kozlowski, Appl. Opt. **32**, 5567 (1993).
20. R. Chow and N. Tsujimoto, Appl. Opt. **35**, 5095 (1996).
21. S. Malobabic, M. Jupe, and D. Ristau, Light-Sci. Appl. **5**, e16044 (2016).
22. Y. N. Zhao, T. Wang, D. P. Zhang, S. H. Fan, J. D. Shao, and Z. X. Fan, Appl. Surf. Sci. **239**, 171 (2005).
23. J. E. Wolfe, S. R. Qiu, and C. J. Stolz, Appl. Opt. **50**, C457 (2011).
24. C. J. Stolz, J. E. Wolfe, J. J. Adams, M. G. Menor, N. E. Teslich, P. B. Mirkarimi, J. A. Folta, R. Soufli, C. S. Menoni, and D. Patel, Appl. Opt. **53**, A291 (2014).
25. X. F. Liu, Y. A. Zhao, D. W. Li, G. H. Hu, Y. Q. Gao, Z. X. Fan, and J. D. Shao, Appl. Opt. **50**, 4226 (2011).
26. X. B. Cheng, T. Ding, W. Y. He, J. L. Zhang, H. F. Jiao, B. Ma, Z. X. Shen, and Z. S. Wang, Proc. SPIE **8190**, 819002 (2011).
27. H. F. Jiao, T. Ding, and Q. A. Zhang, Opt. Express **19**, 4059 (2011).
28. P.-G. Gennes, F. Brochard-Wyart, and D. Quéré, *Capillarity and Wetting Phenomena: Drops, Bubbles, Pearls, Waves* (Springer, 2004).
29. B. Bhushan, *Introduction to Tribology* (Wiley, 2013).
30. C. J. Evans, E. Paul, D. Dornfeld, D. A. Lucca, G. Byrne, M. Tricard, F. Klocke, O. Dambon, and B. A. Mullany, CIRP Ann. **52**, 611 (2003).
31. K. Wakamatsu, S. Kurokawa, T. Toyama, and T. Hayashi, Precis. Eng.-J. Int. Soc. Precis. Eng. Nanotechnol. **60**, 458 (2019).
32. H. Krol, L. Gallais, C. Grezes-Besset, J. Y. Natoli, and M. Commandre, Opt. Commun. **256**, 184 (2005).
33. Y. J. Chai, M. P. Zhu, K. Yi, W. L. Zhang, H. Wang, Z. Fang, Z. Y. Bai, Y. Cui, and J. D. Shao, Opt. Lett. **40**, 3731 (2015).